Electronic Supplementary Information for:

'Exploring quantum phenomena and vibrational control in σ* mediated photochemistry'

Gareth M. Roberts,[a] David J. Hadden,[a] L. Therese Bergendahl,[b] Andreas M. Wenge,[c]

Stephanie J. Harris,[c] Tolga N.V. Karsili,[c] Michael N.R. Ashfold,[c]*

Martin J. Paterson[b],* and Vasilios G. Stavros[a],*

[a] *Department of Chemistry, University of Warwick, Library Road, Coventry, CV4 7AL, UK*

[b] *Institute of Chemical Sciences, Heriot-Watt University, Edinburgh, EH14 4AS, U.K.*

[c] *School of Chemistry, University of Bristol, Bristol, BS8 1TS UK*

*To whom correspondence should be address:

v.stavros@warwick.ac.uk; m.j.paterson@hw.ac.uk; mike.ashfold@bristol.ac.uk

Figures: Fig. S1 – S8

Tables: Tables S1 – S2

S1. Ultrafast Time-resolved Velocity Map Imaging

The ultrafast time-resolved velocity map imaging (TR-VMI) apparatus has been described in detail previously[1] and only an overview is provided here. Thioanisole (Sigma-Aldrich, >99 %) is seeded in ~2 bar of He and introduced into a VMI spectrometer[2] using an Even-Lavie pulsed solenoid valve[3] (repetition rate = 125 Hz) heated to ~60 °C, operating with an opening time of ~13 μs. Dynamics are initiated using femtosecond (fs) laser pulses ($h\nu_{pu}$), centered at wavelengths between 289.8 – 275 nm (~4 – 6 μJ/pulse), generated using an optical parametric amplifier (Light Conversion, TOPAS-C) seeded by a portion of the fundamental 800 nm output (1 mJ/pulse) from a regeneratively amplified Ti:sapphire fs laser system (Spectra-Physics, Spitfire XP). CH_3 radicals in their v = 0 level are subsequently ionized to generate CH_3^+ as a function of pump-probe time delay (Δt), using a temporally delayed fs probe pulse ($h\nu_{pr}$) centered at 333.6 nm (7 μJ/pulse), two photons of which correspond to the origin band of the $3p\left({}^2\mathrm{A}_2''\right) \leftarrow \tilde{\mathrm{X}}\left({}^2\mathrm{A}_2''\right)$ transition in the CH_3 radical.[4] $h\nu_{pr}$ is generated using a second optical parametric amplifier (Light Conversion, TOPAS-C). For these experiments, the Gaussian laser cross-correlation is ~120 fs full width at half maximum (FWHM) at all pump wavelengths, while focused pump and probe pulses have intensities of ~10^{11} and ~10^{13} W cm^{-2}, respectively, at the point of interaction with the molecular beam pulses in the VMI spectrometer. CH_3^+ is detected using TR-VMI, where the position sensitive VMI detector (microchannel plate pair coupled to a phosphor screen and CCD camera) is gated to detect only a specific mass of interest, in this case CH_3^+ (m/z 15), by applying a timed voltage pulse (Behlke). Total kinetic energy release (TKER) spectra at each Δt are derived from the measured CH_3^+ images using a polar onion-peeling algorithm,[5] which also yields a quantitative measure of the photofragment recoil distribution by fitting the signal at each radius of the image, $I(\theta)$, to a second order Legendre polynomial:[6]

$$I(\theta) = \frac{\sigma}{4\pi}\left[1 + \frac{\beta_2}{2}\left(3\cos^2\theta - 1\right)\right] \tag{S1}$$

In eqn (S1), σ is the overall photodissociation cross-section, θ is the photofragment recoil angle with respect to the electric field vector of $h\nu_{pu}$ (ε) and β_2 is the anisotropy parameter. β_2 exhibits limiting values of –1 and +2 in the case that the fragments recoil along an axis that is, respectively, perpendicular ($\theta = 90°$) or parallel ($\theta = 0°$) to the parent electronic transition dipole moment (TDM).

S2. Nanosecond Velocity Map Imaging

The nanosecond (ns) velocity map imaging (VMI) setup used has also been described in detail elsewhere.[7] Briefly, a mixture of thioanisole (Sigma-Aldrich, >99 %) seeded in He (~400 mbar), was supersonically expanded into the vacuum chamber, skimmed and then intersected, at right angles, by two counter propagating laser beams. The first, from a frequency tripled Nd:YAG pumped dye laser (Quanta Ray GCR-250, Sirah Cobra Stretch, KDP-crystal for frequency doubling, 1 mJ/pulse), was set at many different wavelengths in the range of 290 – 283 nm and used to dissociate the molecules. As in the fs experiments, the second, from a frequency doubled Nd:YAG pumped dye laser (Quanta Ray GCR-170, PDL-2, KDP crystal for frequency doubling, ~0.5 mJ/pulse) was tuned to the maximum of the $3p\left({}^{2}\mathrm{A}_{2}''\right) \leftarrow \tilde{\mathrm{X}}\left({}^{2}\mathrm{A}_{2}''\right)$ 0_0^0 two photon absorption band of the CH_3 radical (333.6 nm). All experiments were conducted in the cold front of the molecular beam with a 20 ns time delay between photolysis and probing. The photolysis laser wavelengths readily induce multiphoton dissociation of thioanisole, so the intensity of this laser was maintained as low as possible in order to minimize such undesirable background signal. Ions formed in the interaction region were accelerated with a velocity mapping ion optics assembly, through a field free time-of-flight region, towards a position sensitive detector (double microchannel plates coupled to a phosphor screen and a CCD camera).

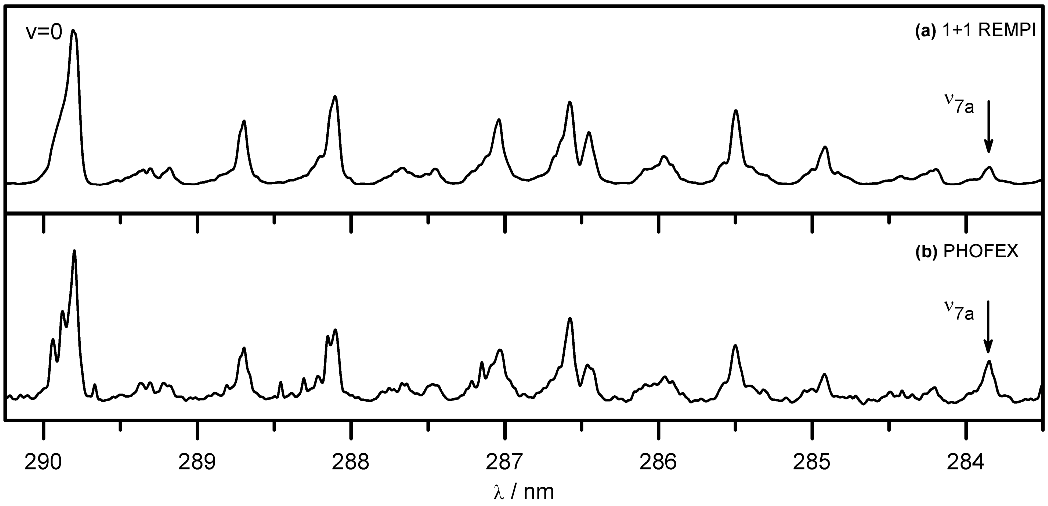

Fig. S1 (a) Parent REMPI and (b) CH_3 radical PHOFEX spectra obtained following ${}^{1}\pi\pi^{*} \leftarrow S_0$ excitation of a jet-cooled thioanisole sample.

Resonances in the parent ${}^{1}\pi\pi^{*} \leftarrow S_0$ excitation spectrum were identified in two ways. The first involved measurement of the 1+1 resonance enhanced multiphoton ionization (REMPI) spectrum of jet-cooled thioanisole by recording the total parent ion signal (m/z 124) as a function of pump laser wavelength (Fig. S1(a)). The second involved recording the excitation spectrum for forming $CH_3(v = 0)$ fragments (monitored by 2+1 REMPI at 333.6 nm) as a function of photolysis wavelength – the so-called photofragment excitation (or PHOFEX) spectrum (Fig. S1(b)). Photofragment images were acquired and processed using an event counting mode (LaVision, DaVis 6.2). Analysis of the recorded ns velocity map images and derivation of TKER spectra was also performed using the polar onion-peeling method,[5] as described for the fs TR-VMI measurements – we note that a selection of velocity map images have also been analyzed using the fitting method outlined in ref. 8, and that the results of both methods are in good agreement.

S3. Fitting TKER Spectra

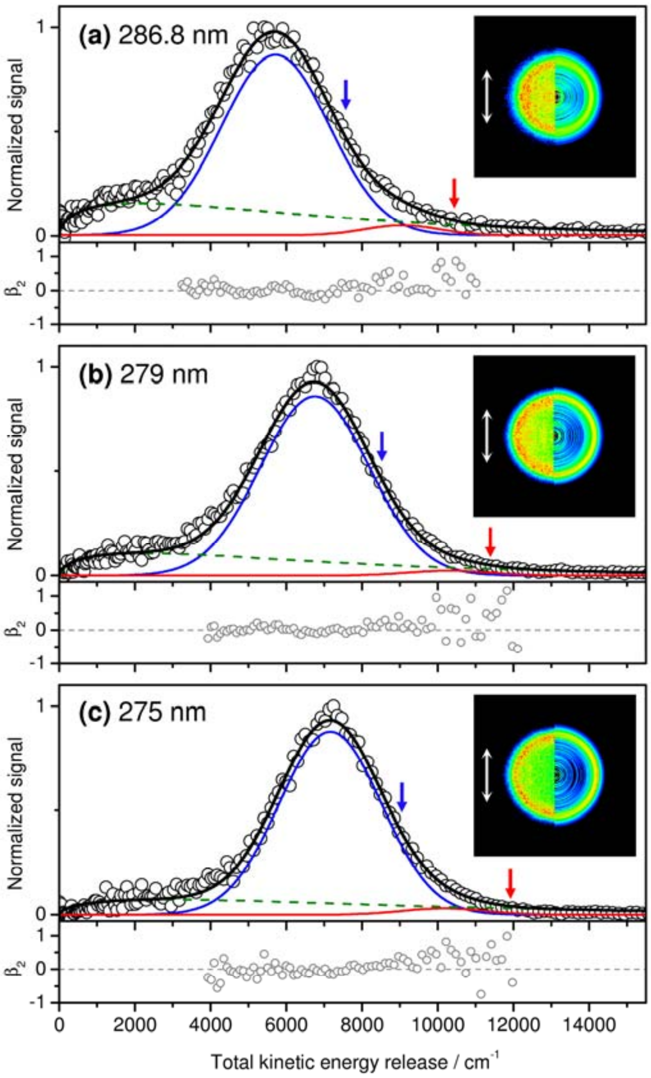

Fig. S2. fs TKER spectra, CH_3^+ velocity map images (inset) and β_2 spectra (bottom) recorded at a pump-probe delay of $\Delta t = 1.2$ ns at pump wavelengths of (a) 289.8, (b) 279 and (c) 275 nm. Left halves of the images present the raw image, while the right halves display a reconstructed deconvoluted slice through the centre of the original 3-D ion distribution. White arrows indicate the electric field polarization, $\boldsymbol{\varepsilon}$, of $h\nu_{pu}$. Solid black lines correspond to fits to the TKER spectra, with individual components of the fit correlating to channel **1** (solid red) and **2** (solid blue) photoproducts and the 'Boltzmann-like' background signal (dashed green). Vertical red and blue arrows indicate the predicted $\mathrm{TKER_{max}}(\tilde{\mathrm{X}})$ and $\mathrm{TKER_{max}}(\tilde{\mathrm{A}})$ values, obtained from eqn (2) and (3) of in the main manuscript, respectively.

The TKER distributions presented in Figs. 2 and 4(b) of the main manuscript (and Fig. S2) are fitted to the sum of two Gaussians and a 'statistical' function, which model the channel **1** and **2** photoproduct signals and the underlying 'Boltzmann-like' features, respectively. The overall fit to the TKER profile, $I(x)$, has the functionality

$$I(x) = I_0 + \left[\frac{A\sqrt{x}}{\exp(x/\rho)}\right] + \left[B\exp\left(-\frac{(x-\mu_1)^2}{2\sigma_1^{\,2}}\right)\right] + \left[C\exp\left(-\frac{(x-\mu_2)^2}{2\sigma_2^{\,2}}\right)\right] \qquad \text{(S2)}$$

where x is the TKER, I_0 is the baseline signal level, A is the amplitude of the statistical function, ρ is the statistical function width, B and C are the Gaussian function amplitudes, μ_n is the centre of the Gaussian distribution n, and σ_n is the width of Gaussian function n. From these fits we are able to extract the centre (mean) TKER of channel **1** and **2** signals, μ_n, at each pump wavelength. Results from these fits, are provided in Table S1 for each excitation wavelength.

Table S1. Extracted center (mean) TKER for channel **1** and **2** signals (μ_1 and μ_2, respectively) from fits to fs and ns TKER spectra with eqn (S2).

	fs TKER spectra		ns TKER spectra	
λ / nm	μ_1 / cm^{-1}	μ_2 / cm^{-1}	μ_1 / cm^{-1}	μ_2 / cm^{-1}
289.8	8586	5582	8597	5813
286.8	9053	5716	…	…
283.9	9688	6203	9398*	6777*
279	10297	6753	…	…
275	10169	7162	…	…

* Values obtained from fits with eqn (S3)

Inspection of the ns TKER spectrum in Fig. 4(a) of the main manuscript reveals that the signal distributions correlating to channel **1** and **2** photoproducts are not well modeled by Gaussian distributions, unlike the other spectra presented. In this case, to capture the profile of the TKER spectrum better, and to enable a more accurate determination of the channel **1**:channel **2** branching ratio, a 'statistical' function in combination with two generalized extreme value (Gumbel) distributions is used, which has the functionality:

$$I(x) = I_0 + \left[\frac{A\sqrt{x}}{\exp(x/\rho)}\right] + \left[B\exp\left(-\frac{(-x+\mu_1)}{\sigma_1}\right)\exp\left\{-\exp\left(-\frac{(-x+\mu_1)}{\sigma_1}\right)\right\}\right] + \left[C\exp\left(-\frac{(-x+\mu_2)}{\sigma_2}\right)\exp\left\{-\exp\left(-\frac{(-x+\mu_2)}{\sigma_2}\right)\right\}\right] \tag{S3}$$

where x is the TKER, I_0 is the baseline signal level, A is the amplitude of the statistical function, ρ is the statistical function width, B and C are the Gumbel function amplitudes, μ_n is a location parameter of Gumbel distribution n, and σ_n is a width parameter of Gumbel function n.

S4. Kinetic Analysis of the CH_3^+ Signal Transients for Channel 2 Products

CH_3^+ signal transients associated with the channel **2** photoproducts are generated by integrating over a 2000 cm^{-1} energy window centered on the feature of interest (μ_2 for fs TKER spectra are provided in Table S1) at each pump-probe delay. Transients are fitted using a combination of: (*i*) a fast exponential rise, $r_1(\Delta t)$, which describes the rapid rise in signal around Δt = 0 picoseconds (ps) corresponding to the appearance of the broad underlying Boltzmann-like signal; and (*ii*) a second exponential rise function, $r_2(\Delta t)$, which models the appearance of REMPI probed CH_3 radicals associated with channel **2** photoproducts. These two functions are each convoluted with the Gaussian instrument response function, $g(\Delta t)$, and have the form:

$$r_n(\Delta t) = g(\Delta t) * \left[1 - A_n \exp\left(-\frac{\Delta t}{\tau_n}\right)\right], \tag{S4}$$

where A_n and τ_n are the amplitudes and time constants associated with exponential rise function *n* and Δt is the pump-probe delay. The overall fit equation, $f(\Delta t)$, is subsequently given as

$$f(\Delta t) = r_1(\Delta t) + r_2(\Delta t). \tag{S5}$$

Fits to all five signal transients (Fig. 5 in the main manuscript) yield τ_1 time constants with values < 50 fs, within the temporal instrument response window of our experiments (~120 fs FWHM). Extracted values for τ_2 are reported in Table 1 of the main manuscript (simply labeled τ).

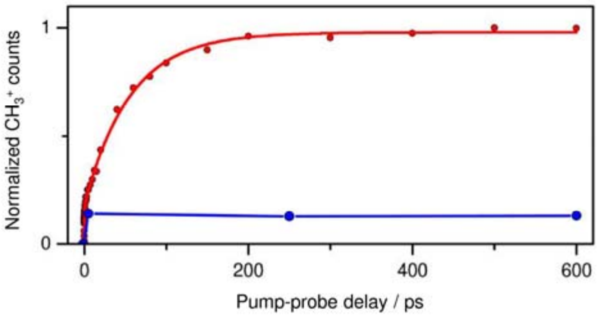

Fig. S3. Example of an integrated CH_3^+ signal transient around the TKER region of the channel **2** feature (6500 – 8500 cm^{-1}) recorded with an 'on' (red, 333.6 nm) and 'off' resonant (blue, 323 nm) fs probe. Both transients are recorded with a 275 nm pump wavelength.

We highlight that detuning the probe wavelength away from the REMPI transition ($\lambda \neq 333.6$ nm) results in negligible long time rise in the recorded signal transients, further confirming that the growing signal results from probing neutral CH_3 radicals associated with channel **2** photoproducts. This is exemplified in Fig. S3, comparing 'on' (333.6 nm) and 'off' (323 nm) resonance signal transients following excitation at 275 nm.

S5. Computational Details

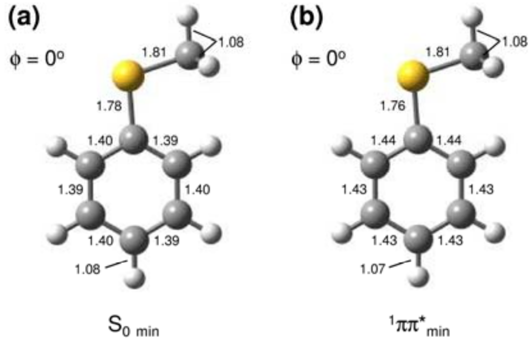

Fig. S4. Calculated minimum energy structures of (a) the S_0 state ($S_{0\ \mathrm{min}}$) and (b) the $^1\pi\pi^*$ state ($^1\pi\pi^*_{\mathrm{min}}$) at the CASSCF(8,7)/6-311G(d) level of theory. Bond lengths (in Å) and torsional angles (ϕ) are also given for the respective structures.

Complete active space self consistent field (CASSCF) calculations were performed using the Gaussian 03 computational suite.[9] The 6-311G(d) Pople basis set is used for all CASSCF calculations. We highlight that the CASSCF method is used here to generate qualitatively correct wavefunctions around the conical intersection (CI) regions of the potential energy landscape, where non-adiabatic dynamics are most probable, as well as at additional nuclear geometries of interest, such as global minima. The minimum energy geometries of the S_0 and $^1\pi\pi^*$ states (Fig. S4) were calculated using an 8 electrons in 7 orbitals (8,7) active space, consisting of the three π orbitals, three π* orbitals and the n_π orbital of the sulfur (orbital hypersurfaces generated in the CASSCF calculations are provided in Fig. S5). This active space generates 490 singlet configuration state functions. Conical intersection (CI) search calculations were performed using a larger (10,9) active space, which additionally contains the σ and σ* orbitals associated with the S–CH_3 bond. This larger active space generates 5292 singlet configuration state functions (without applying C_s spatial symmetries). CI searches were performed using equal state averaging (SA) between the electronic states involved. Further CI optimizations utilizing electronic (C_s) symmetry were performed using a reduced (8,7) active space obtained from the optimized (10,9) one by discarding the most strongly and most weakly occupied active space orbitals (labeled 1π and 3π* in Fig. S5). The orbital rotation derivatives were negated from the solutions of the coupled perturbed multi-configuration self-consistent field equations when performing CI searches with the (10,9) active space but not for the (8,7) space. Force convergence criteria were given careful consideration when interpreting resultant CI structures and calculated S_0 and $^1\pi\pi^*$ minima. We note that the $^1\pi\pi^*$ minimum energy geometry was also determined using the larger (10,9) active space, and found to be very comparable to that obtained using the (8,7) active space.

Time-dependent density functional theory (TD-DFT) using the CAM-B3LYP functional[10] and coupled cluster response calculations were also performed in order to determine vertical excitation energies (Δ*E*), oscillator strengths (*f*) and TDMs for excitation to the singlet excited states of thioanisole using the Gaussian 09[11] and Dalton 2.0[12] packages, respectively. Triplet states were also computed using TD-CAM-B3LYP. The CAM-B3LYP

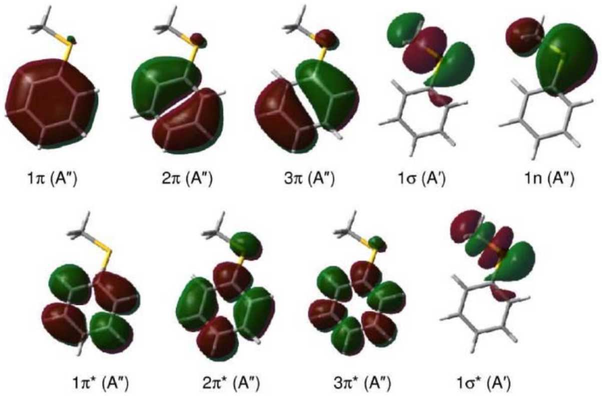

Fig. S5. State-averaged (SA) $^1\pi\pi^*/^1n\sigma^*$ optimized CASSCF orbitals, using a 6-311G(d) basis set.

functional has been selected as we have previously demonstrated its suitability for excited state photochemistry problems in heteroaromatics, comparing particularly well to high level coupled cluster methods.[13] Linear-response coupled cluster single and double excitations (LR-CCSD) and non-iteratively corrected triples (CCSDR(3)) methods were both performed using the aug-cc-pVDZ basis set, while TD-CAM-B3LYP calculations utilized the larger aug-cc-pVTZ basis set. Initial S_0 geometry optimizations for LR-CCSD and CCSDR(3) calculations were performed at the B3LYP/6-31G(d) level, while TD-CAM-B3LYP calculations were fully geometry optimized using CAM-B3LYP/cc-pVTZ. The coupled cluster response method enables a systematic convergence of molecular properties, such as excitation energies, as one expands the single particle basis and *N*-electron space of the correlated wavefunction. Particularly for singly excited states, calculated LR-CCSD excitation energies are fully correct through second order in the fluctuation potential, while CCSDR(3) is a non-iterative approximation of the full third order CC3 model (further details are provided in ref. 14).

S6. Electronic Structure of Thioanisole

A UV absorption spectrum of vapor-phase thioanisole (Fig. S6) was recorded over the range 310 – 240 nm using a commercial UV-Visible absorption spectrometer (Perkin Elmer, Lambda 25, 1 nm resolution) by expanding thioanisole vapor into a fused silica sample cell at room temperature. Guidance for interpreting this spectrum comes from the ΔE and f values determined with LR-CCSD, CCSDR(3) and TD-CAM-B3LYP calculations, which are provided in Table S2. The three sets of calculations are in reasonable agreement with one another, identifying the lowest energy singlet state (S_1) to be of ππ* character – in-line with previous studies[15, 16] – and predicting a vertical excitation energy for the $^1\pi\pi^*$ state in the range 4.70 – 4.95 eV. TD-CAM-B3LYP and LR-CCSD methods both suggest small (and broadly comparable) oscillator strengths (f values) for the $^1\pi\pi^* \leftarrow S_0$ transition. Spectroscopic studies[15, 16] identify the $^1\pi\pi^* \leftarrow S_0$ origin band (*i.e.* the $^1\pi\pi^*(v = 0)$ level) at 4.28 eV (λ_{pu} ~289.8 nm), evident as a small peak in the absorption spectrum shown in Fig. S6 and as a pronounced feature in the parent REMPI spectrum (Fig. S1(a)). The absorption

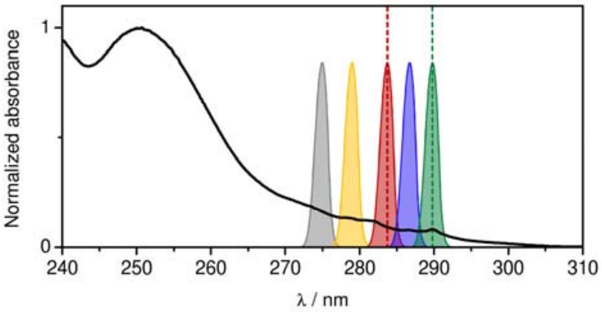

Fig. S6. Vapor-phase UV absorption spectrum of thioanisole recorded over the range 310 – 240 nm (black line). Superimposed on top of the spectrum are the spectral profiles of the fs pulses used in the fs TR-VMI measurements, centered at wavelengths of 289.8 (green), 286.8 (blue), 283.9 (red), 279 (orange) and 275 nm (gray). Dashed lines at 289.8 (green) and 283.9 nm (red) indicate wavelengths used for ns VMI studies.

Table S2. Calculated vertical excitation energies (Δ*E*) obtained at the TD-CAM-B3LYP/aug-cc-pVTZ, LR-CCSD/aug-cc-pVDZ and CCSDR(3)/aug-cc-pVDZ levels of theory for the first three singlet excited states (S_1 – S_3) in thioanisole. Δ*E* for the first four triplet excited states (T_1 – T_4), calculated at the TD-CAM-B3LYP/aug-cc-pVTZ level, are also provided. Where applicable, associated oscillator strengths (*f*) are given in parentheses. Electronic state configurations and symmetries (in the C_s point group) are also provided.

			Δ*E* / eV		
State	Configuration	Symmetry	TD-CAM-B3LYP	LR-CCSD	CCSDR(3)
T_1	ππ*	*A′*	3.42	…	…
T_2	ππ*	*A′*	4.25	…	…
T_3	ππ*	*A′*	4.57	…	…
T_4	nσ*	*A″*	4.83	…	…
S_1	ππ*	*A′*	4.95 (0.0154)	4.80 (0.0075)	4.70
S_2	nσ*	*A″*	5.14 (0.0005)	5.19 (0.0017)	5.14
S_3	ππ*	*A′*	5.31 (0.2311)	5.52 (0.2565)	5.41

spectrum also shows a weak tail stretching to longer wavelengths (to ~305 nm) which we suggest arises from hot band absorptions and, as in thiophenol,[17] from weak absorptions to low lying triplet states (the calculated Δ*E* values for which are also provided in Table S2). The calculations show the S_2 state to be of nσ* character, and to lie 0.19 – 0.44 eV above the vertical onset of the $^1\pi\pi^*(S_1)$ state. TD-CAM-B3LYP and LR-CCSD calculations return an $^1n\sigma^* \leftarrow S_0$ oscillator strength some 4 – 30 times weaker than that of the $^1\pi\pi^* \leftarrow S_0$ transition, suggesting that the ^{1}nσ* state will make (at most) a minor contribution to the measured absorbance in Fig. S6. The present calculations also determine a higher lying ^{1}ππ* state (S_3), with a vertical excitation energy in the range 5.31 – 5.52 eV and an f value one to two orders of magnitude larger than that of the $^1ππ^*(S_1) \leftarrow S_0$ transition (see Table S2). Given that all three linear response theory methods overestimate $\Delta E(^1ππ^*(S_1) \leftarrow S_0)$ (*cf.* the spectroscopic data), we assign the enhanced absorption once $\lambda < 265$ nm in Fig. S6 to $^1ππ^*(S_3) \leftarrow S_0$ excitation, and most of the longer wavelength absorption in the range 290 – 270 nm to the $^1ππ^*(S_1) \leftarrow S_0$ transition. Our ns VMI and fs TR-VMI experiments thus utilize pump wavelengths in the range 289.8 – 275 nm – the approximate spectral profiles of the fs pulses are superimposed on the absorption spectrum in Fig. S6.

S7. Recoil Anisotropies

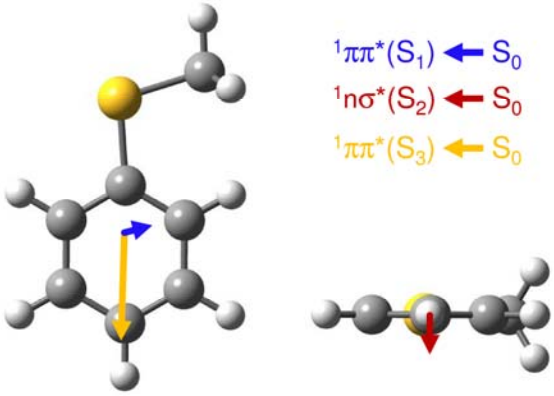

Fig. S7. Calculated TDM vectors for the first three singlet electronic transitions of thioanisole, computed at the TD-CAM-B3LYP/aug-cc-pVTZ level of theory. For clarity the magnitude of the $^1nσ^*(S_2) \leftarrow S_0$ TDM vector is scaled by a factor of ×20 relative to the $^1ππ^*(S_1) \leftarrow S_0$ and $^1ππ^*(S_3) \leftarrow S_0$ TDM vectors.

Analysis of the ns velocity map images in the main manuscript (Figs. 2(a) and 4(a)) returns positive β_2 parameters (0.4) for all channel **1** and **2** products, notwithstanding the fact that the deduced dissociation lifetime (~1.4 ns when exciting at the $^1ππ^*(S_1)$-S_0 origin) is much longer than the parent rotational period. This is not an experimental artifact – images taken with ε perpendicular to the front face of the detector show the expected azimuthal symmetry – and can be rationalized as follows. As noted in the main manuscript, the minimum energy geometries of the S_0 and $^1ππ^*(S_1)$ states of thioanisole have the S–CH_3 bond lying in the phenyl ring plane (see Fig. S4), essentially parallel to the $^1ππ^*(S_1) \leftarrow S_0$ TDM (see Fig. S7). Were dissociation to be prompt following excitation to $^1ππ^*(S_1)$, we should thus expect a CH_3 fragment recoil velocity distribution characterized by $\beta_2 \sim 2$. The excited state is long lived, however, and parent rotation will degrade the alignment of the molecular plane in the laboratory frame by (up to) a factor of 4 following excitation with a ns laser pulse.[18] The recoil anisotropy of the CH_3 fragments is likely to be further degraded by the requirement that $\phi > 0°$ (*i.e.* the S–CH_3 bond is directed out of the ring plane) in order to facilitate non-adiabatic coupling to the ^{1}nσ* PES (see main manuscript). The asymptotic trajectories of the

CH_3 fragments will be further influenced by the topography of the $^1n\sigma^*$ PES, however, and the magnitude of the β_2 parameters determined in the ns images (~0.4) implies that the ultimate recoil velocity vectors of most CH_3 fragments lie fairly close to the ring plane.

The fs images, in contrast, show no obvious recoil anisotropy ($\beta_2 \sim 0$). Saturation of the pump or probe transition would be one possible reason for non-observation of recoil anisotropy, but images recorded at the lowest possible pump and probe intensities were similarly isotropic. The $^1\pi\pi^*(S_1) \leftarrow S_0$ and $^1n\sigma^*(S_2) \leftarrow S_0$ TDMs are orthogonal to one another (see Fig. S7); the latter is also orthogonal to the S–CH_3 bond in the planar equilibrium geometry. In principle, therefore, a seemingly isotropic recoil velocity distribution could be obtained by 'superposing' components arising from both types of electronic excitation. However, the calculated $^1\pi\pi^*(S_1) \leftarrow S_0$ TDM magnitude is much larger than that for the $^1n\sigma^*(S_2) \leftarrow S_0$ transition (see Table S2 and Fig. S7), and we have not been able to record any ns images with negative recoil anisotropy by exciting at wavelengths between the $^1\pi\pi^*(S_1) \leftarrow S_0$ resonances in the CH_3 PHOFEX spectrum.

fs excitation of thioanisole yields a ro-vibrational wavepacket on $^1\pi\pi^*(S_1)$.[19] Broadband fs pulses will therefore generate a *coherent* ensemble of rotational states in $^1\pi\pi^*(S_1)$, as previously demonstrated by Felker and Zewail.[20, 21] These rotational coherences will evolve as a function of time, leading to their rapid de-phasing and an isotropically distributed ensemble of molecules in their $^1\pi\pi^*(S_1)$ state.[20-22] This rapid scrambling of the rotational coherences (on a timescale faster than S-CH_3 bond dissociation), coupled to the fact that molecules in $^1\pi\pi^*(S_1)$ must also evolve to a nuclear geometry where $\phi > 0°$ for S-CH_3 fission to occur, offers one explanation for the isotropic nature of the fs velocity map images. In principle, one may anticipate some temporal evolution of the β_2 parameter for the channel **2** feature in TR-VMI measurements (*cf.* ultrafast time-resolved photoelectron imaging[22, 23]). However, rotational de-phasing clearly takes place on a timescale faster that S-CH_3 bond fission between 289.8 – 275 nm excitation (see extracted dissociation rates in Table 1 of main manuscript), resulting in negligible CH_3 signal associated with channel **2** products at early time delays, ultimately precluding any obvious observation of temporal changes to β_2 around (and immediately following) $\Delta t = 0$. Furthermore, as the initial superposition of rotational states is coherent, one may expect to observe rotational (molecular alignment) revivals in the excited ensemble of $^1\pi\pi^*(S_1)$ state molecules.[23-25] However, no distinct evidence for this is observed in the TR-VMI experiments.

S8. Calculated Conical Intersection Topographies

In an effort to understand the topography of the $^1n\sigma^*/S_0$ CI (CI2) in the $R_{S\text{-}CH_3}$ and ϕ plane more clearly, we have performed CI geometry optimizations restricted at $\phi = 90°$. These calculations do not locate any points of degeneracy between $^1n\sigma^*$ and S_0 at $\phi = 90°$, suggesting that the topography of the $^1n\sigma^*/S_0$ CI, as a function of $R_{S\text{-}CH_3}$ and ϕ is conical, with the minimum energy crossing point located at $\phi \approx 0°$. Additional analysis of the

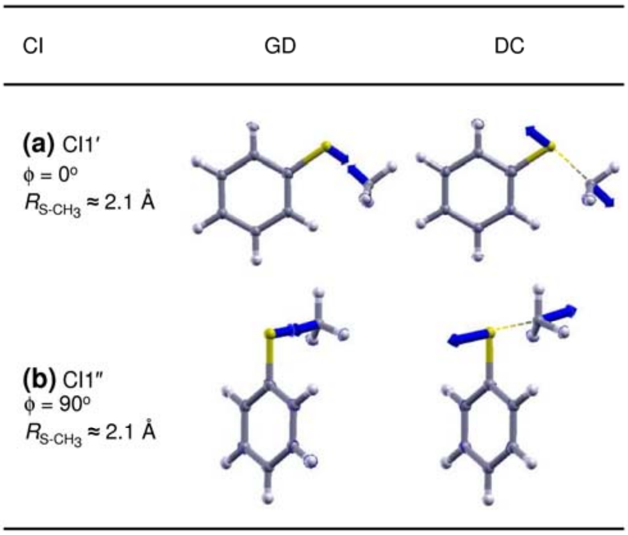

Fig. S8. Calculated gradient difference (GD) and derivative coupling (DC) branching space vectors for (a) CI1′ and (b) CI1″, without C_s symmetry enforced, at the CASSCF(10,9)/6-311G(d) level of theory.

CASSCF CI search results can also enable further insight into the topographies of CI ‘seams’ in thioanisole.

Examination of the upper and lower state gradients in the vicinity of CI2 show that it has a ‘peaked’ topography in the terminology of Ruedenberg and co-workers,[26] as the gradients are almost exactly orthogonal to each other. Inspection of the forces and average geometric displacement in the CI2 search indicates that the conical profile around this region of the surface is particularly shallow, likely due to the fact that the energy difference between the asymptotic limits of the $^1n\sigma^*$ and S_0 states, corresponding the $\tilde{A} \leftarrow \tilde{X}$ excitation energy in the C_6H_5S radical co-fragments, is only ~3000 cm^{-1}.[27]

Unlike CI2, a similar analysis of the state gradients of the $^1\pi\pi^*/^1n\sigma^*$ quasi-CI seam (CI1′ and CI1″) is ‘sloped’.[26] as determined by examining the upper and lower state gradients in the vicinity of the intersection and noting that they are very close to being parallel. Additionally, CI search calculations with the (10,9) active space, without C_s symmetry restrictions enforced, where also conducted. The branching spaces obtained for CI1′ and CI1″ from these calculations are presented in Fig. S8, and are discussed in more detail in the main manuscript.

ESI References

1. K. L. Wells, G. Perriam and V. G. Stavros, *J. Chem. Phys.*, 2009, **130**, 074304.
2. A. T. J. B. Eppink and D. H. Parker, *Rev. Sci. Instrum.*, 1997, **68**, 3477-3484.
3. U. Even, J. Jortner, D. Noy, N. Lavie and C. Cossart-Magos, *J. Chem. Phys.*, 2000, **112**, 8068-8071.
4. J. W. Hudgens, T. G. Digiuseppe and M. C. Lin, *J. Chem. Phys.*, 1983, **79**, 571-582.
5. G. M. Roberts, J. L. Nixon, J. Lecointre, E. Wrede and J. R. R. Verlet, *Rev. Sci. Instrum.*, 2009, **80**, 053104.

6. R. N. Zare, *Angular Momentum: Understanding Spatial Aspects in Chemistry and Physics*, Wiley, New York, 1988.
7. E. Wrede, S. Laubach, S. Schulenburg, A. Brown, E. R. Wouters, A. J. Orr-Ewing and M. N. R. Ashfold, *J. Chem Phys.*, 2001, **114**, 2629-2646.
8. A. M. Wenge, U. Kensy and B. Dick, *Phys. Chem. Chem. Phys.*, 2010, **12**, 4644-4655.
9. *Gaussian 03*, Revision D.01, M. J. Frisch, G. W. Trucks, H. B. Schlegel, G. E. Scuseria, M. A. Robb, J. R. Cheeseman, J. A. Montgomery, Jr., T. Vreven, K. N. Kudin, J. C. Burant, J. M. Millam, S. S. Iyengar, J. Tomasi, V. Barone, B. Mennucci, M. Cossi, G. Scalmani, N. Rega, G. A. Petersson, H. Nakatsuji, M. Hada, M. Ehara, K. Toyota, R. Fukuda, J. Hasegawa, M. Ishida, T. Nakajima, Y. Honda, O. Kitao, H. Nakai, M. Klene, X. Li, J. E. Knox, H. P. Hratchian, J. B. Cross, V. Bakken, C. Adamo, J. Jaramillo, R. Gomperts, R. E. Stratmann, O. Yazyev, A. J. Austin, R. Cammi, C. Pomelli, J. W. Ochterski, P. Y. Ayala, K. Morokuma, G. A. Voth, P. Salvador, J. J. Dannenberg, V. G. Zakrzewski, S. Dapprich, A. D. Daniels, M. C. Strain, O. Farkas, D. K. Malick, A. D. Rabuck, K. Raghavachari, J. B. Foresman, J. V. Ortiz, Q. Cui, A. G. Baboul, S. Clifford, J. Cioslowski, B. B. Stefanov, G. Liu, A. Liashenko, P. Piskorz, I. Komaromi, R. L. Martin, D. J. Fox, T. Keith, M. A. Al-Laham, C. Y. Peng, A. Nanayakkara, M. Challacombe, P. M. W. Gill, B. Johnson, W. Chen, M. W. Wong, C. Gonzalez, and J. A. Pople, Gaussian, Inc., Wallingford CT, 2004
10. T. Yanai, D. P. Tew and N. C. Handy, *Chem. Phys. Lett.*, 2004, **393**, 51-57.
11. *Gaussian 09*, Revision A.02, M. J. Frisch, G. W. Trucks, H. B. Schlegel, G. E. Scuseria, M. A. Robb, J. R. Cheeseman, G. Scalmani, V. Barone, B. Mennucci, G. A. Petersson, H. Nakatsuji, M. Caricato, X. Li, H. P. Hratchian, A. F. Izmaylov, J. Bloino, G. Zheng, J. L. Sonnenberg, M. Hada, M. Ehara, K. Toyota, R. Fukuda, J. Hasegawa, M. Ishida, T. Nakajima, Y. Honda, O. Kitao, H. Nakai, T. Vreven, J. A. Montgomery, Jr., J. E. Peralta, F. Ogliaro, M. Bearpark, J. J. Heyd, E. Brothers, K. N. Kudin, V. N. Staroverov, R. Kobayashi, J. Normand, K. Raghavachari, A. Rendell, J. C. Burant, S. S. Iyengar, J. Tomasi, M. Cossi, N. Rega, J. M. Millam, M. Klene, J. E. Knox, J. B. Cross, V. Bakken, C. Adamo, J. Jaramillo, R. Gomperts, R. E. Stratmann, O. Yazyev, A. J. Austin, R. Cammi, C. Pomelli, J. W. Ochterski, R. L. Martin, K. Morokuma, V. G. Zakrzewski, G. A. Voth, P. Salvador, J. J. Dannenberg, S. Dapprich, A. D. Daniels, Ö. Farkas, J. B. Foresman, J. V. Ortiz, J. Cioslowski, and D. J. Fox, Gaussian, Inc., Wallingford CT, 2009.
12. DALTON, a molecular electronic structure program, Release 2.0 (2005), see http://www.kjemi.uio.no/software/dalton/dalton.html 2005.
13. G. M. Roberts, C. A. Williams, J. D. Young, S. Ullrich, M. J. Paterson and V. G. Stavros, *J. Am. Chem. Soc.*, 2012, **134**, 12578-12589.
14. O. Christiansen, *Theor. Chem. Acc.*, 2006, **116**, 106-123.
15. M. Hoshino-Nagasaka, T. Suzuki, T. Ichimura, S. Kasahara, M. Baba and S. Kawauchi, *Phys. Chem. Chem. Phys.*, 2010, **12**, 13243-13247.
16. J. S. Lim and S. K. Kim, *Nature Chem.*, 2010, **2**, 627-632.
17. A. L. Devine, M. G. D. Nix, R. N. Dixon and M. N. R. Ashfold, *J. Phys. Chem. A*, 2008, **112**, 9563-9574.
18. H. Kim, K. S. Dooley, S. W. North, G. E. Hall and P. L. Houston, *J. Chem. Phys.*, 2006, **125**, 133316.
19. A. H. Zewail, *J. Phys. Chem. A*, 2000, **104**, 5660-5694.
20. P. M. Felker and A. H. Zewail, *J. Chem. Phys.*, 1987, **86**, 2460-2482.
21. J. S. Baskin, P. M. Felker and A. H. Zewail, *J. Chem. Phys.*, 1987, **86**, 2483-2499.

22. D. A. Horke, A. S. Chatterley and J. R. R. Verlet, *J. Phys. Chem. Lett.*, 2012, **3**, 834-838.
23. M. Tsubouchi, B. J. Whitaker, L. Wang, H. Kohguchi and T. Suzuki, *Phys. Rev. Lett.*, 2001, **86**, 4500-4503.
24. P. M. Felker, J. S. Baskin and A. H. Zewail, *J. Phys. Chem.*, 1986, **90**, 724-728.
25. C. Z. Bisgaard, O. J. Clarkin, G. R. Wu, A. M. D. Lee, O. Gessner, C. C. Hayden and A. Stolow, *Science*, 2009, **323**, 1464-1468.
26. G. J. Atchity, S. S. Xantheas and K. Ruedenberg, *J. Chem. Phys.*, 1991, **95**, 1862-1876.
27. J. B. Kim, T. I. Yacovitch, C. Hock and D. M. Neumark, *Phys. Chem. Chem. Phys.*, 2011, **13**, 17378-17383.